[1] J. Galindo, R. Navarro, D. Tarí, F. Moya, Development of an experimental test bench and a psychrometric model for assessing condensation on a Low Pressure EGR cooler, Internation Journal of Engine Researchdoi:10.1177/1468087420909735.

Development of an experimental test bench and a psychrometric model for assessing condensation on a Low Pressure EGR cooler

J. Galindo[a], R. Navarro[a], D. Tarí[a], F. Moya[a,*]

[a] *CMT - Motores Térmicos, Universitat Politècnica de València*
Camino de Vera, 46022 Valencia

Abstract

A test bench has been designed to assess condensation formation produced on the interior of a Low Pressure EGR cooler working with hot stream of humid air representing an engine warm up stage, when its coolant starts from very cold conditions. An experimental campaign has been conducted with three different EGR mass flow rates, four EGR inlet temperatures and three different coolant initial temperatures, covering common conditions found in the Low Pressure EGR system of internal combustion engines under cold starts. The transient experimental results are analyzed and compared with a simple psychrometric condensation model, obtaining a good correlation and reproducing the trends of the condensation, even though an overprediction of the condensates of around 20-40 % exists due to the strong hypotheses assumed. The warm-up tests are most sensitive to the initial coolant temperature. For example, an engine starting at -10 °C ambient

*Corresponding author. Tel.: +34 963 877 650
Email addresses: galindo@mot.upv.es (J. Galindo), ronagar1@mot.upv.es (R. Navarro), datade@mot.upv.es (D. Tarí), framoto1@mot.upv.es (F. Moya)

temperature could require 10 minutes to stop producing water in the LP-EGR cooler, with an accumulated quantity during the warm-up of about 100 ml of condensates.
Keywords: Low-Pressure EGR, Experimental setup, Engine warm-up, Heat exchanger, WLTC, Engine cold start

1. Introduction

Light-duty vehicles play an important role in modern societies [1], improving the mobility of people and goods [2]. As a result, the vehicle fleet has increased significantly during the last decades, generating or increasing issues which were not a concern some time ago, including the pollution produced by the manufacturing process and usage of internal combustion engines (ICE) [3]. With a production of 98.9 million units (European Automobile Manufacturers Association (ACEA) [4]) only in 2017, any improvement in the reduction of ICE emissions would became a positive contribution to the world.

Due to the direct correlation between the emissions produced and the environmental impact [5], stringent emission regulations have been introduced around the world.

Pollution regulations are steadily becoming more restrictive. It is widely known that the Worldwide harmonized Light vehicles Test Cycle (WLTC) [6] will consider low and realistic winter temperatures as boundary conditions [7]. Under these conditions, pollutant emissions are mainly emitted during the warm-up of the engine [8, 9].

Emissions reduction technologies are divided into active (in-cylinder) or

passive (aftertreatment control measurements) [10]. In-cylinder control systems functioning is based in the reduction of pollutants within the source. For example controlling the injection scheme (pressure, duration...), using Exhaust Gas Recirculation (EGR) [11] or injecting water into the cylinders [12, 13]. This work is focused on using EGR as an emission reduction technique [14]. This technique consists in recirculating a portion of the exhaust gases back to the engine cylinders mixed with fresh air, which dilutes the concentration of O_2 and provides inert gases to the combustion process. This reduces the in-cylinder peak temperature and, therefore, the NOx emissions [15].

Considering a turbocharged engine, two possible paths of EGR are available, depending on location of extraction and reintegration of the exhaust gases. The most commonly used technique (as in 2020) is the so-called High-Pressure EGR (HP-EGR) which connects the exhaust and the intake manifolds. The other path available is the Low-Pressure EGR (LP-EGR), which consists in taking the exhaust gases downstream the aftertreatment and reintroducing them before the compressor.

Low pressure EGR presents several advantages over HP-EGR. Lapuerta et al. [14] concluded that LP-EGR is more efficient than HP-EGR to reduce NOx emissions, mainly due to the higher recirculation potential and the lower temperature of the recirculated gas; for this reason, the LP-EGR has attracted much research in the last years [16, 17, 18]. Another difference between both alternatives is related with the mass flow rate (MFR) that goes through the turbine and the compressor. When the LP-EGR is activated, the flow passing through the turbocharger is not affected. Conversely, with

the HP-EGR, the flow going throw the turbocharger is reduced, generating lower efficiency values and reducing the compressor surge margin [19]. From the point of view of air charge, using LP-EGR produces an intake manifold temperature reduction compared with the HP-EGR, which positively affects the fuel consumption [20]. Finally, another important aspect is the cylinder-to-cylinder EGR distribution. The mixing of the LP-EGR gases and fresh air is produced upstream the compressor and far away from the cylinders, allowing a perfect distribution of the exhaust gases inside the cylinders. On the other hand, the HP-EGR system may not be able to uniformly distribute the exhaust gases in the cylinders due to closeness of the EGR discharge to the intake pipes. This phenomenon is responsible for cylinder charge non-uniformities [21, 22], which increase NOx or particulate matter emissions.

To cope with the pollution issue, an early activation of the LP-EGR system during the engine warm-up could be a solution in order to fulfill the emission regulations at those boundary conditions. However, a drawback appears when using a LP-EGR at low engine temperatures. Water condensation may be produced in two different localizations; first in the LP-EGR path, specially in the cooler due to the low temperature of the walls and the coolant during the warm-up of the engine [23, 24, 25]. In addition, it can be found in the mixing region between fresh air and EGR gas, due to its high water content [26, 27]. Water droplets can produce an important damage to the compressor impeller, severely reducing its durability. In other research fields such as steam jets [28, 29] or nozzles [30], water condensation is also a problem.

Authors such as (Noori [31], Murphy [32] or Vasyliv [33]) have studied

the phenomena of in-flow condensation, but with another gases (propane or steam) instead of most air. Regarding the condensation in EGR coolers, Warey et al. [34] provided a surface condensation model for the EGR cooler. Whereas Cuevas et al. [35] conducted an experimental campaign on LP-EGR cooler to assess condensation, but in steady conditions.

The aim of this research is to assess the implications of using the LP-EGR system during the warm-up of an automotive cycle, in terms of condensation in the LP-EGR cooler. The first novelty of this work is the development of an experimental test bench to quantify the condensation on a heat exchanger, while other authors such as Lujan et al. [36] only were able to study the condensation in a qualitative way. The advantages and the limitations of the test rig will be addressed as well. The analysis of water generation covers the operating range of a C-segment passenger car into the future taking into account regulations, in which, an early activation of the LP-EGR will be required. Finally, a development of a simple mean value condensation model is shown based on a psychrometric analysis. During the development of this work, the LP-EGR cooler performance was evaluated under transient conditions to emulate the thermal inertia and the warm-up of the engine coolant of the engine. In sequence, a weighing scale was added after the LP-EGR cooler to quantify the evolution of the water generation. At last, a detailed analysis of the tests and the comparison with the model was performed to assess the impact of using a LP-EGR system during the cold conditions of an early activation.

In Section 2, the developed experimental test bench and the condensation model are explained. Next, the measured condensation rate for different

working points is presented in Section 3, together with the results predicted by the model. Finally, the conclusions obtained are exposed in Section 4.

2. Materials and methods

2.1. Experimental apparatus

In order to assess the condensation produced in the LP-EGR cooler, a continuous flow test rig has been used to replicate engine exhaust conditions, reducing, thus, the complexity of an actual Internal Combustion Engine (ICE) test bench. In this way, humid air will be used instead of exhaust gases with unburned hydrocarbons, particles matter. The difference related with the condensation produced between using an ICE or a flow test rig is low, as assessed in Appendix A.1 with a deviation between 1-4% in terms of accumulated water. The flow test rig layout is depicted in Fig. 1.

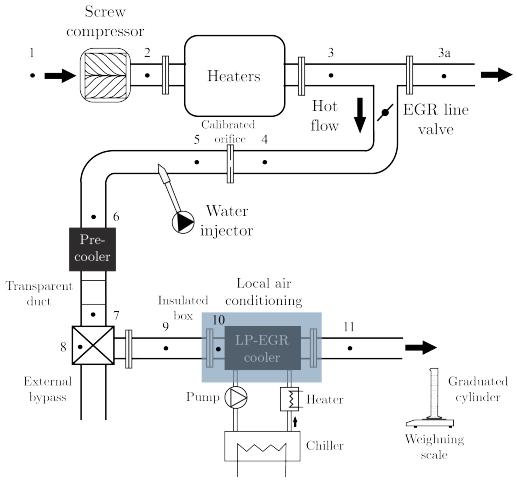

Figure 1: Scheme of the LP-EGR cooler condensation test rig with the stations.

As will be presented in Section 2.2, with this arrangement it is possible to reproduce the transient operating range of a LP-EGR cooler during an

engine warm-up and also to arrive to any operative point of a wide range of common steady operating points from both medium and light duty ICEs.

At the core of the rig, there is an Atlas Copco ZE 3C-300-5E VSD volumetric screw compressor (between stations 1 to 2 of Fig 1), which is able to provide up to 720 kg/h of mass flow and a maximum pressure of 4 bars. This compressor is connected to five heaters (Watlow, 9 kW each) (between stations 2 to 3) to increase the flow temperature to 400 °C, in order to guarantee a complete evaporation of the water injected downstream. A counter-pressure valve controls the mass flow rate circulating through the flow test rig.

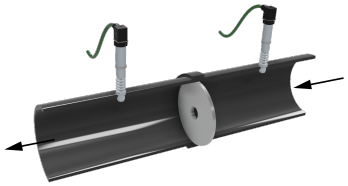

Figure 2: Calibrated orifice.

Because of the high flow temperature and the water content, it is complex to measure the mass flow rate. For this reason, it was decided to employ a calibrated orifice (Fig. 2). The mass flow meter described in Table 1 was previously employed to characterize the relation between pressure drop and MFR of the orifice. Equation 2 shows how the target EGR humid MFR is calculated to be imposed in the calibrated orifice. This target depends on the desired MFR, the ambient conditions, and the specific humidity (w) of the EGR gas.

$$\dot{m}_{orif} = \dot{m}_{EGR} \cdot \frac{1 - w_{EGR}}{1 - w_{amb}} \tag{1}$$

$$\dot{m}_{inj} = \dot{m}_{EGR} \cdot \frac{w_{EGR} - w_{amb}}{1 - w_{amb}} \tag{2}$$

After the orifice, a *Bosch AdBlue dosing module denoxtronic 2.1 injector* is placed, which adds the desired water content. An arduino board [37] controls the injection rate using a pulse-width modulation (PWM) signal. The operating range of the injector is between 0 and 3 l/h, which limits the maximum specific humidity that can be set. A further constraint over EGR humidity is the maximum quantity of water that the flow is able to evaporate (dependent of the MFR). In order to make sure the evaporation of the water content occurs, 3 extra meters of pipe are installed between the injector and the next element. A calibration of the injector is performed which correlates the water injection rate with the duration pulse lengths of the PWM signal in order to be able to set the exact water quantity at the tests. Then, a weighing scale is set in the water reservoir to measure and double-check the water injection. Next, a pre-cooler is installed to control the temperature of the flow required for each specific test. In order to check that the flow is not condensing in the pre-cooler, a transparent duct is installed on its outlet to visualize the presence of liquid water. Between points 7 and 9 of Fig. 1, a bypass is mounted in order to allow a proper settling of the flow temperature when the target cooler is placed in the insulated box, prior to start measuring.

This insulated box features a local air conditioning as shown in Fig. 3. Inside the box, there are the following elements: a radiator with a fan in order to set a cold ambient in the box and the target LP-EGR cooler, both connected through the coolant line. This coolant line is connected to a heater,

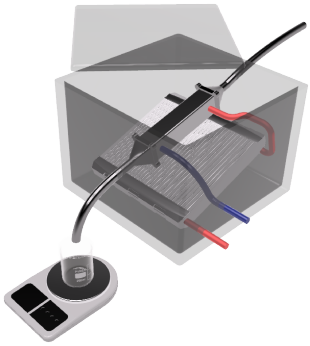

Figure 3: Local air conditioning.

Table 1: Instrumentation accuracy[1]

Sensor	Model	Accuracy [
Thermocouples	Thermocouple K-type WATLOW	1
Pressure sensor	Piezoresistive KISTLER RAG25A52BV1H	0.3
Flow meter	ABB SENSYCON 14241-5-7962633	1
Weighting scale for water injection	Balance AND GX-20K	0.1
Weighting scale for condensation MFR	Balance AND EK-300i	0.001

[1] According to datasheets

a chiller and a pump. The chiller is an Euroklimat M10 MICRO with 3.75 kW of nominal cooling capacity. Inside the chiller, there is a pump that moves coolant (ethylene glycol 30 % - water 70 %) in the coolant circuit through the LP-EGR cooler, the radiator, the heater and the chiller. Finally, in order to simulate warm-up conditions, a 5 kW heater is set in the coolant line to obtain an approximation of the WLTC coolant temperature profile, which will control the condensation produced in the LP-EGR line. At the beginning of the test, once all parameters are stabilized, the bypass valve is closed and

the flow is redirected towards the cooler in the insulated box. Then, the chiller is switched off and the heater switched on. The outlet of the LP-EGR discharges on a reservoir which collects the fraction of condensed water travelling as large droplets, not being able to collect the tiny droplets existing as fog inside the stream. In any case, the fog generates less damage if arriving to the compressor. The condensed water is measured using a weighing scale connected with a data acquisition system, as can be seen in Fig. 3.

Piezoresistive pressure sensors are mounted along the different ducts of the rig. Their specifications are noted in Table 1. For the temperature sensors, K-type thermocouples are used. The two different weighing scales employed in the test rig, one for obtain the condensation produce in the cooler and the other to check the correct functioning of the injector, are shown as well in Table 1.

Table 2 shows the operating range of the flow test rig with the current setup, being mainly constrained by the ability of the EGR stream to fully evaporate the spray of injected water.

Table 2: Flow test rig - operating range

EGR Temperature[1]	40–180 °C
EGR flow	10–50 kg/h
Specific Humidity	0–65 g/kg
Coolant temperature	-15–60 °C
Local air conditioning	-15–60 °C

[1] Temperature at the pos. 8 of the test rig.

2.2. Operating conditions

As it is mentioned in the introduction, the purpose of the work performed is to assess the impact of the condensation generation during the warm-up, considering the WLTC cycle as a reference to obtain the boundary conditions.

Figure 4 shows the specific humidity during the first 10 minutes of a WLTC cycle comparing with the EGR mass flow rate that is being introduced on a diesel engine for a C-segment passenger car (1.6 L) and the speed of the WLTC cycle. The specific humidity is calculated with the Air-Fuel ratio knowing surrogate C_8H_{15}. Knowing these values and considering the operating range capabilities of the test rig showed in the Table 2, a test matrix is able to be defined in a way that covers a wide range of common operating conditions for a low and medium loads, being specified in Table 2.2. In Section 3, the proposed test matrix will be processed to assess the produced condensation. Only the initial stage of a WLTC cycle was analyzed since the coolant temperature being under the dew point. For the current test, a specific humidity of 46 g/kg is selected as a characteristic and conservative value (dashed black line at Fig. 4).

Concerning the initial coolant temperature, three values are selected: -10, -2.5 and 5 °C (Table 2.2). Figure 5 shows the coolant temperature evolution of the warm-up tests with a 5kW heater, compared with the coolant temperature evolution of a WLTC cycle. The test with the coldest initial temperature (-10 °C) takes near 10 minutes to reach the dew temperature ($\approx$ 40 °C) like in the engine WLTC cycle. Condensation in the LP-EGR cooler is only produced during this period.

Taking into account the results observed at Fig. 4, three different mass

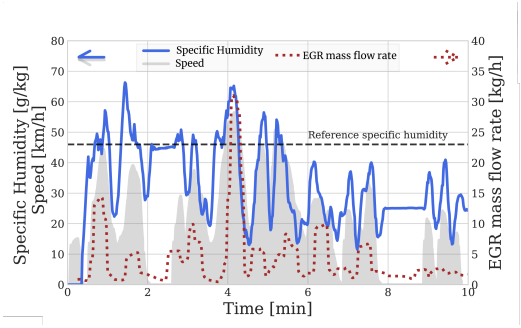

Figure 4: The evolution in time during the WLTC cycle of the specific humidity vs EGR mass flow rate compared with speed.

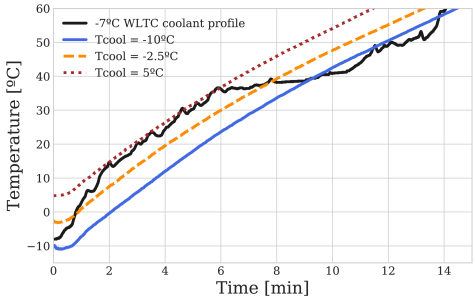

Figure 5: Different coolant temperature evolution during the WLTC cycle using a 5 kW heater compared with an engine coolant evolution.

flow rates are selected: 10, 20 and 40 kg/h (Table 2.2). A higher value than the one shown in Fig.4 (40 kg/h) has been selected considering a future increase of EGR rate, to be able to anticipate futures tightening of the emission requirements.

Finally, in order to cover different EGR temperatures at the inlet of the LP-EGR cooler, four different values are selected (Table 2.2): 45, 70, 90 and 150 °C. These EGR temperature values have been measured during the tests (Position 7 in Fig. 1).

Table 3: Operating points

EGR Temperature[1]	45, 70, 90 and 150 °C
EGR flow	10, 20 and 40 kg/h
Specific Humidity	46 g/kg
Initial coolant temperature	-10, -2.5 and 5 °C
Initial local air conditioning	-10, -2.5 and 5 °C

[1] Temperature at the pos. 8 of the test rig.

2.3. Condensation model in LP-EGR cooler

The simple condensation model proposed in this work does not take into account the local wall temperature in the LP-EGR cooler, the cooler capacity to retain water inside, which delays condensation appearance at the cooler outlet, the partial evaporation and the possible icing generation.

Condensation in the LP-EGR cooler is an undesired phenomenon. Water droplets appear whenever the local gas temperature is below dew temperature. If these droplets are dragged by the EGR flow, the compressor impeller may be damaged [38]. Condensation depends on the gas temperature at the cooler outlet, the heat exchange across the cooler and the dew point of the LP-EGR flow. More in detail, the dew temperature depends on the specific humidity and, to a lesser degree, the gas pressure. In Eq. 3, Serrano et al. [38] defined a correlation of the dew temperature with the RH and the temperature.

$$T_{dew} = \sqrt[8]{\frac{RH}{100}} \cdot (112 + 0.9 \cdot T) + (0.1 \cdot T) - 112 \tag{3}$$

Figure 6 shows the moisture air psychometric diagram, in which the inlet

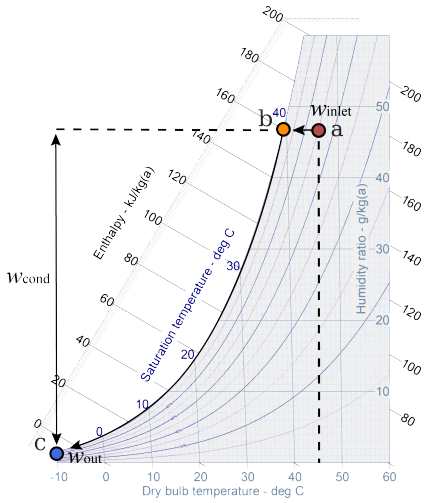

Figure 6: Psychrometric diagram with the ideal evolution between points a to c.

and outlet conditions for a given point (T_{inlet}=45 °C, T_{out}=-10 °C, w_{inlet}=46 g/kg) have been represented. Point (a) is cooled down until saturated conditions (b). Then, cooling continues and the point follows the curve RH=100% defined by Eqs. 4, 5, 6 until it achieves the outlet temperature (c).

$$p_{vap} = \frac{p_{gas}}{1 + 1000\dfrac{MW_{H2O}}{w_i \cdot MW_{dryair}}} \tag{4}$$

$$p_{sat} = 10^{4.6543 - \dfrac{1435.264}{T_{gas} + 273.15 - 64.848}} \tag{5}$$

$$RH = \frac{p_{vap}}{p_{sat}} \cdot 100 \tag{6}$$

The model only considers the cooler outlet temperature of each time step for the water condensation prediction. The estimation of the humidity that has condensed (Eq. 7) at each time step (same as sampling time), being w_i

the saturation specific humidity at each time step, is given by:

$$w_{cond}(t) = \frac{w_{EGR}(t) - w_i(t)}{1 + \frac{w_{EGR}(t)}{1000}} \tag{7}$$

$$\dot{m}_{cond} = w_{cond} \cdot \dot{m}_{dryair} \tag{8}$$

$$m_{cond}(warm - up//test) = \int_0^{T_{test}} \dot{m}_{cond} \cdot dt \tag{9}$$

The Equations 8 and 9 are used to calculate the accumulation of condensed water since the beginning of the test. As aforementioned, the wall temperature in the LP-EGR cooler which could be locally below the gas outlet temperature, is not taken into account due to the 0D approximation. The cooler capacity to retain water inside is not considered due to the geometrical complexity of each specific design, then neglecting the delays produced by the soak capacity of the cooler that presents some of the condensates to come out of the cooler. Other phase change phenomena are not considered either, such as evaporation and icing.

3. Results and discussion

The results are divided into three subsections. The first subsection (3.1) shows the pressure and temperature evolution during the beginning of the test. In the second subsection (3.2), the condensation rate produced during the warm-up test is compared with the model results developed in section 2.3. Finally, the last subsection (3.3) presents the total amount of condensates for the proposed test matrix and the time in which the test takes to finish the production of condensates.

3.1. Pressure and Temperature evolution

In order to evaluate the changes in the boundary conditions due to the start of the test and related with the methodology employed, a test is carried out and the evolution of pressure and temperature are assessed. Figure 7a shows the pressure evolution before and after the starting of the test; when the test starts, the pressure downstream the orifice rises due to the higher pressure drop that causes the LP-EGR cooler compared to the external by-pass valve is activated. Consequently, and following the nozzle equation (Eq.10), Figure 7b shows a reduction in the theoretical mass flow rate close to the 2 % for the cases with the higher amount of MFR, which agrees with a value of $C_D \simeq 1$ in Eq.10 for the calibrated orifice as was obtained by a 3D-CFD simulation.

$$\dot{m}_{theo} = A_{orif} \cdot C_D \cdot \frac{p_{04}}{\sqrt{R \cdot T_{04}}} \cdot \sqrt{\frac{2 \cdot \gamma_{air}}{\gamma_{air} - 1} \cdot \left(\frac{p_5}{p_{04}}\right)^{\frac{2}{\gamma_{air}}} - \left(\frac{p_5}{p_{04}}\right)^{\frac{\gamma_{air}+1}{\gamma_{air}}}} \tag{10}$$

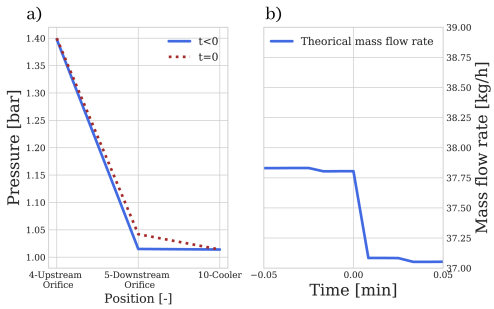

Figure 7: Evolution of pressure and MFR in the the flow test rig for $t < 0$ and $t > 0$.

The temperature evolution for the working point with an initial coolant temperature of -10 °C, mass flow rate of 20 kg/h and EGR temperature of 70

°C is shown in the Fig. 8. The evolution temperature is represented in two instants: at $t < 0$ and at time t_{dew}, when the cooler outlet exceeds the dew temperature (Eq. 11). The EGR mass flow temperature is being considered as the position 8 in the test rig (see Fig. 1) in order to procedure with the setup of the installation previously on the test.

$$T_{11}(t = t_{dew}) = T_{dew,10}; \quad T_{dew,10} = T_{dew,10}(w_{init}, P_{11}) \tag{11}$$

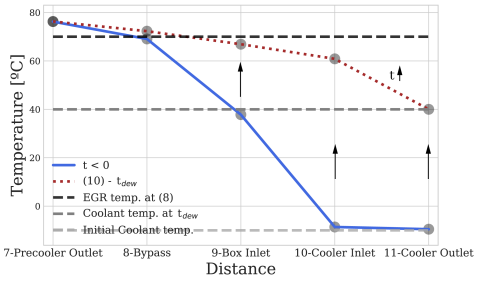

Figure 8: Temperature evolution at different points of the test rig for $t < 0$ and $t > 0$ at T_{cool}= -10 °C $\dot{m}$=20 kg/h and T_{EGR} = 70 °C.

Notice that the test starts with ($T_{10} = T_{11} = T_{cool,init}$) and, after that, the temperatures 9 (Box inlet), 10 (Cooler inlet) and 11 (Cooler outlet) begin to increase (Fig. 8). Looking at the difference between cooler inlet and outlet temperature, the time-dependent EGR cooler efficiency can be calculated.

3.2. Condensation rate

Some comparisons of the condensation rate produced during the warm-up tests with the estimation of the model developed in section 2.3 are shown in Figures 9, 10 and 11. In order to process the measurements obtained by the weighing scale, one has to take into account the extra weight measured due

to the discharge flow momentum (see Appendix A.2). Moreover, a partial derivative of the measured condensation weight trace is performed to obtain the condensation rate and a running mean average is used.

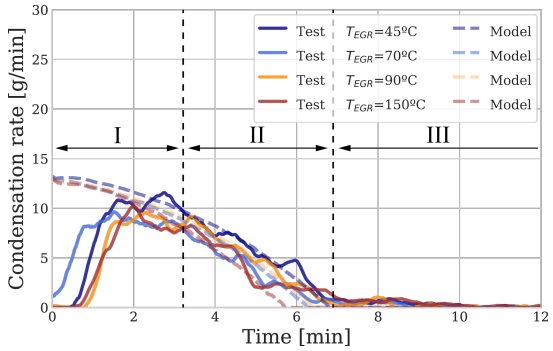

Figure 9: Condensation rate evolution during time for $\dot{m}$=20 kg/h, T_{cool}=5 °C and modifying T_{EGR}.

In first place, Fig. 9 shows the tests with different EGR temperature at a mass flow rate of 20 kg/h and at an initial coolant temperature of 5 °C. As can be seen, three noticeable stages are outstanding in the figure. On one hand, the first stage (Stage I) where the condensates starts and where the difference between the test and the model prediction is maximum. In the second stage (Stage II), the measured and modeled condensation rate are similar, decreasing due to the increasing coolant temperature, and ends when the theoretical condensation stops (t_{dew} from Eq. 11). On the other hand, the third stage (Stage III) ends when the actual condensation is stopped.

Compared with the previous figure, Fig. 10 shows the tests with a mass flow rate of 20 kg/h and a coolant temperature of -10 °C. The most noticeable difference in Stage I is the possibility of distinguish two parts. Stage Ia considers the period until the condensation is detected at the cooler outlet.

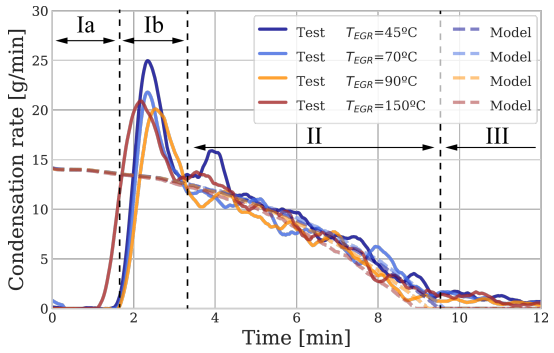

Figure 10: Condensation rate evolution during time for $\dot{m}$=20 kg/h, T_{cool}=-10 °C and modifying T_{EGR}.

Then, in the Stage Ib some condensation rate peaks appear caused by the formation of ice inside the cooler during the first minutes of the test (temperatures below 0 °C) followed by its melting and a sudden release through the cooler outlet to the weighing scale.

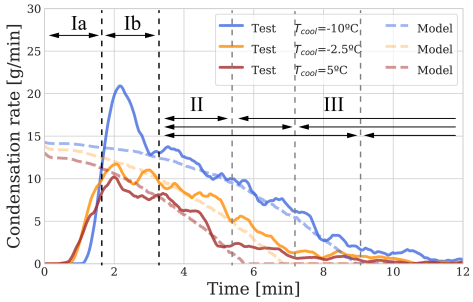

Figure 11: Condensation rate evolution during time for $\dot{m}$=20 kg/h, T_{EGR}=150 °C and modifying T_{cool}.

Finally, Fig. 11 shows, for the same mass flow rate ($\dot{m}$=20 kg/h) and EGR temperature (T_{EGR}=150 °C), some tests modifying the initial coolant temperature (T_{cool}) between values of -10 to 5 °C. As can be seen, when com-

paring with the previous figures, the difference appears between the length of the Stages II and III. For each test, the time t_{dew} in which the cooler outlet exceeds the dew temperature is different because of the initial coolant temperature of each test. Thus, Stage II increases its length with the reduction of T_{cool}.

3.3. Accumulated condensation map

The accumulated condensates produced during the warm-up approximations for the cases of 20 kg/h are presented in Figs. 12 and 13, which represent the experimental results and the predictions of the model, respectively.

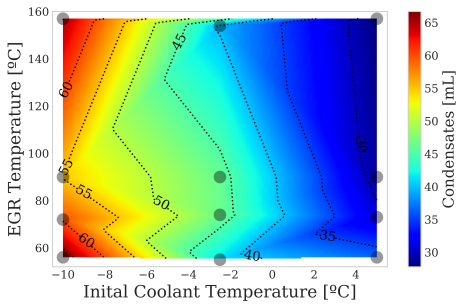

Figure 12: Final condensates at 20 kg/h, experimentally measured.

Starting with the experimental results, Fig. 12 shows the accumulated condensates depending on the EGR temperature (position 8 in Fig. 1) (for $t < 0$) and the initial coolant temperature. As aforementioned, the key parameter that controls the generated condensation is the coolant temperature, which produces higher condensates as it decreases. In fact, due to the high efficiency of the LP-EGR cooler, the impact of the EGR temperature is quite low, as can be seen in the figure.

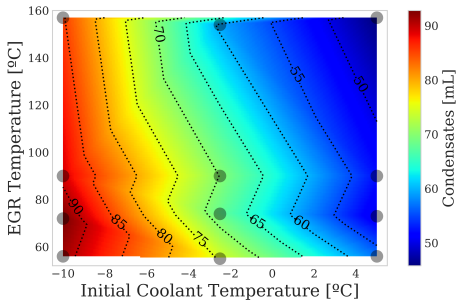

Figure 13: Final condensates at 20 kg/h obtained by the model.

Concerning the model prediction, Fig. 13 shows a result analogous to the previous figure but with an overprediction of the condensates of around 20-40 %. The trends found in the experimental figure are captured by the model. As exposed in Section 2.3, the model only considers the cooler outlet temperature of each time step for the water condensation prediction. Thus, differences appear due to the simplified thermal modelling of the cooler which implies an underestimation of the condensates due to neglecting some phenomena such as the presence of cold spots inside the cooler below dew conditions.

Regarding t_{dew} in which the production of condensates stops, as it is mentioned in Eq. 11, notable differences are observed between mass flow rates, coolant temperatures and EGR temperatures. In Fig. 14, the time until the condensation stops is shown for all mass flow rates and initial coolant temperature at a EGR temperature of 90 °C. There are not significant differences between EGR temperatures, but discrepancies appear between different initial coolant temperatures and, in a smaller scale, between mass flow rates. The greater the reduction on the initial coolant temperature, the longer the

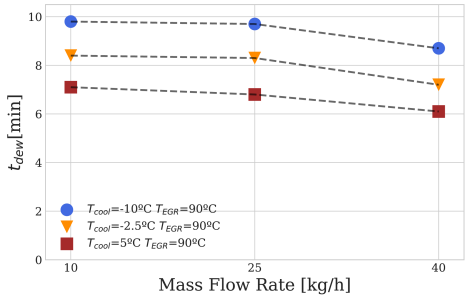

Figure 14: Time to finish the condensates compared with the mass flow rates for a T_{EGR} = 90 °C and different coolant temperatures.

time to finish the condensation produced in the LP-EGR cooler. Comparing by mass flow rates, some differences appear due to the aforementioned effect of the cooler efficiency, with a higher amount of MFR, and an increase of thermal load occurs, being able to reduce the t_{dew}.

4. Conclusions

The effects of low ambient temperature on condensation formation inside the LP-EGR cooler are analysed in this work, thanks to the experimental setup proposed for this task. Experimental tests were carried out on simulating the warm-up transient evolution of a WLTC cycle in a flow test rig.

Regarding the condensation produced, different behaviors were observed. On the one hand, the coolant temperature takes the key role in the condensation production, a lower initial coolant temperature produces a higher condensation rate and accumulated water at the end of the test. On the other hand, the gas inlet temperature and the MFR gas have a noticeable but lower influence on the condensation production due to the modification

of the cooler efficiency, i.e., as the MFR increases, a non-ideal cooler is not able to cool down the gas until the coolant temperature, thus reducing the condensed water. Moreover, a relevant tendency appears in the cases of a coolant temperature of -10 °C. Ice forms inside the cooler at the beginning of the warm-up and is later rapidly melted and expelled through the outlet.

Concerning the condensation model presented in this article, the predicted results are consistent with the experimental tests, except at the very beginning of the test. This error is produced due to not considering the local wall temperature in the LP-EGR cooler, the cooler capacity to retain water inside, the partial evaporation and the icing produced in the cases of coolant temperature below 0 °C.

Finally, regarding the time until the condensation stops (t_{dew}), a strongly dependence of the coolant temperature has been found as well. The inlet gas temperature and the mass flow rate, which lower the efficiency as they rise, also reduce the time to stop the condensation.

The experimental setup has some limitations regarding the maximum gas mass flow rate and water injection rate that can be achieved. Nevertheless, the requirements for simulating a C-segment passenger car diesel engine are covered. In order to simulate heavy duty engine conditions, an upgrade should be applied to the test rig including more water injectors.

Future works on this topic are addressed to develop an advanced condensation model with a higher accuracy. A proper model should consider local wall temperature distribution and partial evaporation.

5. Acknowledgements

The authors of this paper wish to thank Alejandro Hernndez Salmern for his invaluable work during the laboratory setup and the experimental campaign. Francisco Moya is partially supported through a FPI-GVA-ACIF-2019 grant of the Government of Generalitat Valenciana and the European Social Fund.

List of Symbols

A	Area	m^2
C_D	discharge coefficient	$-$
c_D	drag coefficient	$-$
c_p	isobaric specific heat capacity	$J \cdot kg^{-1} \cdot K^{-1}$
dt	time variation	s
F	Force	N
h	enthalpy	$J \cdot kg^{-1} \cdot K^{-1}$
MW	molecular weight	$kg \cdot mol^{-1}$
$\dot{m}$	mass flow rate	$kg \cdot s^{-1}$
p	pressure	Pa
R	specific gas constant	$J \cdot kg^{-1} \cdot K^{-1}$
RH	relative humidity	%
T	temperature	K
u	velocity	$m \cdot s^{-1}$
w	specific humidity	$g_{H_2O} \cdot kg_{air}^{-1}$
γ	ratio of specific heats	$-$
ρ	density	$kg \cdot m^{-3}$

[1] R. D. Reitz, H. Ogawa, R. Payri, T. Fansler, S. Kokjohn, IJER editorial: The future of the internal combustion engine, International Journal of engine Research 21 (2020) 0–8. doi:10.1177/1468087419877990.

[2] M. Dalla Chiara, B. Pellicelli, Sustainable road transport from the energy and modern society points of view: Perspectives for the automotive industry and production, Journal of cleaner production 133 (2016) 1283–1301. doi:10.1016/j.jclepro.2016.06.015.

[3] P. Prevedouros, L. Mitropoulos, Life Cycle Emissions and Cost Study of Light Duty Vehicles, Transportation Research Procedia 15 (2016) 749–760. doi:10.1016/j.trpro.2016.06.062.

[4] The Automobile industry Pocket Guide, 2018-2019.
URL https://www.acea.be/uploads/publications/ACEA_Pocket_Guide_2018-2019.pdf

[5] M. Tutuianua, P. Bonnela, B. Ciuffoa, T. Haniub, N. Ichikawac, A. Marottaa, J. Pavlovica, H. Stevend, Development of the Worldwide harmonized Light duty Test Cycle (WLTC) and a possible pathway for its introduction in the European legislation, Transportation Research Part D: Transport and Environment 40 (2015) 61–75. doi:10.1016/j.trd.2015.07.011.

[6] M. Andre, The ARTEMIS European driving cycles for measuring car pollutant emissions, Science of The Total Environment 334-335 (2004) 73–84. doi:10.1016/j.scitotenv.2004.04.070.

[7] P. Olmeda, J. Martín, F. Arnau, S. Artham, Analysis of the energy balance during World harmonized Light vehicles Test Cycle in warmed and cold conditions using a Virtual Engine, International Journal of Engine Research - (2020) 0–18. doi:10.1177/1468087419878593.

[8] J. M. Luján, H. Climent, L. M. García-Cuevas, A. Moratal, Pollutant emissions and diesel oxidation catalyst performance at low ambient temperatures in transient load conditions, Applied Thermal Engineering 129 (2018) 1527 – 1537. doi:10.1016/j.applthermaleng.2017.10.138.

[9] K. Jinyoung, S. Jeonghun, M. Cha-Lee, P. Simsoo, Comparative study on low ambient temperature regulated/unregulated emissions characteristics of idling light-duty diesel vehicles at cold start and hot restart, Fuel. 233 (2018) 620–631. doi:10.1016/j.fuel.2018.05.144.

[10] K. Fotis, S. Kim, S. Shobhana, C. Thomas, Modeling and optimization of integrated exhaust gas recirculation and multi-stage waste heat recovery in marine engines, Energy Conversion and Management 151 (2017) 286–295. doi:10.1016/j.enconman.2017.09.004.

[11] D. Jung, I. Hwang, Y. Jo, C. Jang, M. Han, M. Sunwoo, J. Chang, In-cylinder pressure-based convolutional neural network for real-time estimation of low-pressure cooled exhaust gas recirculation in turbocharged gasoline direct injection engines, International Journal of Engine Research - (2020) 0–12. doi:10.1177/1468087419879002.

[12] A. Raut, J. M. Mallikarjuna, Effects of direct water injection and injector configurations on performance and emission characteristics of a

gasoline direct injection engine: A computational fluid dynamics analysis, International Journal of Engine Research - (2020) 0–21. doi:10.1177/1468087419890418.

[13] M. Pamminger, B. Wang, C. Hall, R. Vojtech, T. Wallner, The impact of water injection and exhaust gas recirculation on combustion and emissions in a heavy-duty compression ignition engine operated on diesel and gasoline, International Journal of Engine Research - (2020) 0–19. doi:10.1177/1468087418815290.

[14] M. Lapuerta, A. Ramos, D. Fernandez-Rodriguez, I. Gonzalez-Garcia, High-pressure versus low-pressure exhaust gas recirculation in a Euro 6 diesel engine with lean-NOx trap: Effectiveness to reduce NOx emission, International Journal of Engine Research - (2018) 0–9. doi:10.1177/1468087418817447.

[15] A. Ramos, J. Munoz, F. Andres, O. Armas, NOx emissions from diesel light duty vehicle tested under NEDC and real-word driving conditions, Transportation Research Part D: Transport and Environment 63 (0) (2018) 37–48. doi:10.1016/j.trd.2018.04.018.

[16] J. M. Luján, C. Guardiola, B. Pla, A. Reig, Switching strategy between HP (high pressure)-and LPEGR (low pressure exhaust gas recirculation) systems for reduced fuel consumption and emissions, Energy 90 (2015) 1790–1798. doi:10.1016/j.energy.2015.06.138.

[17] S. Moroz, G. Bourgoin, J. M. Luján, B. Pla, Acidic condensation in low

pressure EGR systems using diesel and biodiesel fuels, SAE Int. J. Fuels Lubr 2009-01-2805. doi:10.4271/2009-01-2805.

[18] D. T. Hountalas, G. C. Mavropoulos, K. B. Binder, Effect of exhaust gas recirculation (EGR) temperature for various EGR rates on heavy duty DI diesel engine performance and emissions, Energy 33 (2) (2008) 272–283. doi:10.1016/j.energy.2007.07.002.

[19] J. M. Luján, H. Climent, R. Novella, M. E. Rivas-Perea, Influence of a low pressure EGR loop on a gasoline turbocharged direct injection engine, Applied Thermal Engineering 89 (2015) 432–443. doi:10.1016/j.applthermaleng.2015.06.039.

[20] P. Michel, A. Charlet, G. Colin, Y. Chamaillard, G. Bloch, C. Nouillant, Optimizing fuel consumption and pollutant emissions of gasoline-HEV with catalytic converter, Control Engineering Practice 61 (2017) 198 – 205. doi:10.1016/j.conengprac.2015.12.010.

[21] A. Maiboom, X. Tauzia, J.-F. Hétet, Influence of EGR unequal distribution from cylinder to cylinder on NOx–PM trade-off of a HSDI automotive Diesel engine, Applied Thermal Engineering 29 (10) (2009) 2043 – 2050. doi:10.1016/j.applthermaleng.2008.10.017.

[22] A. Sakowitz, M. Mihaescu, L. Fuchs, Flow decomposition methods applied to the flow in an IC engine manifold, Applied Thermal Engineering 65 (1–2) (2014) 57–65. doi:10.1016/j.applthermaleng.2013.12.082.

[23] M. Weilenmann, J.-Y. Faves, R. Alvarez, Cold-start emissions of modern passenger cars at different low ambient temperatures and their evolution

over vehicle legislation categories, Atmospheric Environment 43 (2009) 2419–2429. doi:10.1016/j.atmosenv.2009.02.005.

[24] J. Bishop, M. Stettler, N. Molden, A. Boies, Engine maps of fuel use and emissions from transient driving cycles, Applied Energy 183 (2016) 202–217. doi:10.1016/j.apenergy.2016.08.175.

[25] Z. Wei, X. Jinliang, L. Guohua, Multi-channel effect of condensation flow in a micro triple-channel condenser, International Journal of Multiphase Flow 34 (2008) 1175–1184. doi:10.1016/j.ijmultiphaseflow.2008.05.004.

[26] J. R. Serrano, P. Piqueras, R. Navarro, D. Tarí, C. M. Meano, Development and verification of an in-flow water condensation model for 3D-CFD simulations of humid air streams mixing, Computers & Fluids 167 (2018) 158 – 165. doi:10.1016/j.compfluid.2018.02.032.

[27] J. Galindo, P. Piqueras, R. Navarro, D. Tarí, C. M. Meano, Validation and sensitivity analysis of an in-flow water condensation model for 3D-CFD simulations of humid air streams mixing, International Journal of Thermal Sciences 136 (2018) 410–419. doi:10.1016/j.ijthermalsci.2018.10.043.

[28] X. Yang, J. Liu, P. Fu, N. Chen, J. Wei, Experimental and theoretical study of pressure oscillation of unstable steam-air jet condensation in water in a rectangular channel, International Journal of Multiphase Flow 119 (2019) 14–27. doi:10.1016/j.ijmultiphaseflow.2019.07.009.

[29] L. Seungho, C. Jinho, L. Haneol, K. Taejoon, S. Weon, Understanding the condensation process of turbulent steam jet using the PDPA system, International Journal of Multiphase Flow 98 (2018) 168–181. doi:10.1016/j.ijmultiphaseflow.2017.09.007.

[30] D. Hongbing, W. Chao, C. Chao, Experimental and numerical studies on self-excited periodic oscillation of vapor condensation in a sonic nozzle, Experimental Thermal and Fluid Science 68 (November 2015) 288–299. doi:10.1016/j.expthermflusci.2015.05.002.

[31] N. Rahim, W. Davies, P. Hrnjakbc, J. Meyera, Numerical study of steam condensation inside a long inclined flattened channel, International Journal of Heat and Mass Transfer 134 (2019) 450–467. doi:10.1016/j.ijheatmasstransfer.2019.01.063.

[32] D. Murphy, M. Macdonald, A. Mahvi, S. Garimella, Condensation of propane in vertical minichannels, International Journal of Heat and Mass Transfer 137 (2019) 1154–1166. doi:10.1016/j.ijheatmasstransfer.2019.04.023.

[33] Y. Vasyliv, D. Lee, R. Tower, Ted. Ng, V. Polashock, A. Alexeed, Modeling condensation on structured surfaces using lattice Boltzmann method, International Journal of Heat and Mass Transfer 136 (2019) 196–212. doi:10.1016/j.ijheatmasstransfer.2019.02.090.

[34] A. Warey, D. Long, S. Balestrino, P. Szymkowcz, Visualization and Analysis of Condensation in Exhaust Gas Recirculation Coolers, in: SAE International Paper, 2013. doi:10.4271/2013-01-0540.

[35] C. Cuevas, D. Makaire, P. Ngendakumana, Thermo-hydraulic characterization of an automotive intercooler for a low pressure EGR application, Applied Thermal Engineering 31 (2011) 2474–2484. doi:10.1016/j.applthermaleng.2011.04.013.

[36] J. M. Luján, V. Dolz, J. Monsalve-Serrano, M. A. Bernal, High-pressure exhaust gas recirculation line condensation model of an internal combustion diesel engine operating at cold conditions, International Journal of Engine Research - (2020) 0–10. doi:10.1177/1468087419868026.

[37] Z. Akram, Ali. Zachary, Open Source Building Science Sensors (OSBSS): A low-cost Arduino-based platform for long-term indoor environmental data collection, Building and Environmental 100 (May 2016) 114–126. doi:10.1016/j.buildenv.2016.02.010.

[38] J. R. Serrano, P. Piqueras, E. Angiolini, C. Meano, J. De La Morena, On Cooler and Mixing Condensation Phenomena in the Long-Route Exhaust Gas Recirculation Line, in: SAE Technical Paper, 2015. doi:10.4271/2015-24-2521.

Appendix A.

Appendix A.1. Humid air vs exhaust gas usage

A calculation has been made in order to assess the impact of using clean air in the test rig instead of engine exhaust gases on the condensation produced. Equation 4 is used to calculate the vapor partial pressure in which the molecular weight (MW) of the dry gas is considered. The MW of dry air

is around 28.96 g/mol, whereas that of diesel engine dry exhaust gas considering a surrogate C_8H_{15} is around 30.46 g/mol. Then, Eq. 5 provides the partial saturation pressure correlation (Antoine equation) of saturated water vapor, which only depends on the temperature of the gas. So, the relation of the RH (Eq. 6) between both gases is connected through a proportional constant as can be seen in Eq. A.1. The error of using this consideration has been assessed using the developed condensation model, resulting in a deviation between 1–4% in terms of accumulated water at the end of the warm-up tests for the selected test matrix, which is in the order of magnitude of the measurement uncertainties.

$$RH_{air} = 0.9543 \cdot RH_{Exh.} \tag{A.1}$$

Appendix A.2. Weighing correction

During the condensation measurements, the cooler outlet discharges over the weighing scale (Fig. 3), increasing the weight measured due to the impact of the flow momentum in accordance with Eq. A.2.

$$F = \frac{1}{2} \cdot c_D \cdot \rho \cdot A \cdot u^2 \tag{A.2}$$

Figure A.15 shows the accumulated condensates as measured (solid line). Notice how the effect of the momentum is observed as a sudden step as the initial flow discharges into the scale and an opposite effect at the end of the discharge ($t_{init} \leq t \leq t_{end}$). This phenomenon significantly distorts the condensation measurement, because the impact of the discharge flow on the scale is time-dependent, as c_D from Eq. A.2 changes with the height of the

condensed column. Equation A.3 shows a linear correction used to subtract the overestimated weight produced by this force. Figure A.15 depicts how this postprocess corrects this spurious additional weight.

$$m_{corr.}(t) = m_{meas.}(t) - \left(m_{init} + \frac{m_{end} - m_{init}}{t_{init} - t_{end}} \cdot (t - t_{init}) \right), \quad t_{init} \leq t \leq t_{end} \tag{A.3}$$

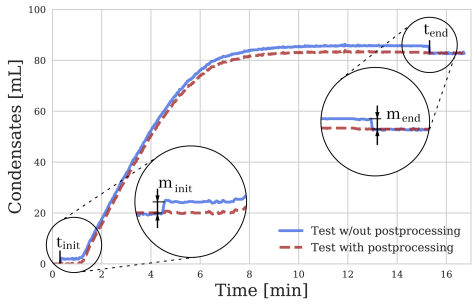

Figure A.15: condensates w/out vs with postprocessing.

Sub- and Superscripts

0	stagnation operating point
$1, 2, 3...$	position in the test rig
$a, dis.$	condensate after the discharge
air	air flow
$amb.$	ambient conditions
$b, dis.$	condensate before the discharge
air	air flow
$cond$	condensates
$cool$	coolant conditions
$corr.$	condensates corrected
dew	dew point
$dryair$	dry air flow
EGR	egr flow
end	end value of the test
$Exh.$	Engine exhaust gas
gas	gaseous flow
H_2O	liquid water
i	data for each time step
$init$	initial value of the test
$inlet$	inlet flow
m	mass
$meas.$	condensates measured
out	outlet flow
sat	saturation
$theo$	theoretical conditions
vap	water vapor
water	liquid water

List of abbreviations

EGR	Exhaust gas recirculation
ICE	Internal combustion engine
LP-EGR	Low-pressure EGR
HP-EGR	High-pressure EGR
MFR	Mass flow rate
NOx	Nitrogen oxides
PWM	Pulse-width modulation
RH	Relative humidity
WLTC	Worldwide harmonized light vehicles test cycle
WLTP	Worldwide harmonized light vehicles test procedure